


Energetics of a bouncing drop: Coefficient of restitution, bubble entrapment, and escape

Cite as: Phys. Fluids **32**, 112107 (2020); <https://doi.org/10.1063/5.0029484>

Submitted: 15 September 2020 . Accepted: 25 October 2020 . Published Online: 16 November 2020

Praveen K. Sharma, and  Harish N. Dixit



View Online



Export Citation



CrossMark

ARTICLES YOU MAY BE INTERESTED IN

[Experimental investigation of a nonspherical water droplet falling in air](#)

Physics of Fluids **32**, 112105 (2020); <https://doi.org/10.1063/5.0031642>

[Effect of charge convection on gravitational settling of drop in uniform electric field](#)

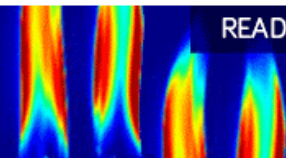
Physics of Fluids **32**, 112013 (2020); <https://doi.org/10.1063/5.0026265>

[Correction and improvement of a widely used droplet–droplet collision outcome model](#)

Physics of Fluids **32**, 111705 (2020); <https://doi.org/10.1063/5.0029463>

AIP Advances
Fluids and Plasmas Collection

READ NOW



Energetics of a bouncing drop: Coefficient of restitution, bubble entrapment, and escape

Cite as: Phys. Fluids 32, 112107 (2020); doi: 10.1063/5.0029484
Submitted: 15 September 2020 • Accepted: 25 October 2020 •
Published Online: 16 November 2020



Praveen K. Sharma and Harish N. Dixit^{a)} 

AFFILIATIONS

Department of Mechanical and Aerospace Engineering, Indian Institute of Technology Hyderabad, Kandi, Sangareddy 502285, India

^{a)} Author to whom correspondence should be addressed: hdixit@mae.iith.ac.in

ABSTRACT

Drops bouncing on an ultra-smooth solid surface can either make contact with the surface or be supported on a thin cushion of gas. If the surface is superhydrophobic, either complete or partial rebound usually occurs. Recent experiments have shed light on the lubrication effect of the underlying gas layer at the onset of impact. Using axisymmetric direct numerical simulations, we shed light on the energetics of a drop bouncing from a solid surface. A complete energy budget of the drop and the surrounding gas during one complete bouncing cycle reveals a complex interplay between various energies that occur during impact. Using a parametric study, we calculate the coefficient of restitution as a function of Reynolds and Weber numbers, and the results are in good agreement with the reported experiments. Our simulations reveal that the Weber number, not the Reynolds number, has a stronger effect on energy losses as the former affects the shape of the drop during impact. At higher Weber and Reynolds numbers, a tiny gas bubble gets trapped inside the drop during impact. We show that a large amount of dissipation occurs during the bubble entrapment and escape process. Finally, analysis of the flow field in the underlying gas layer reveals that maximum dissipation occurs in this layer, and a simple scaling law is derived for dissipation that occurs during impact.

Published under license by AIP Publishing. <https://doi.org/10.1063/5.0029484>

I. INTRODUCTION

Understanding the dynamics of drop impact near a solid surface offers insights into a diverse range of applications ranging from ink-jet printing^{1,2} to heat transfer through spray cooling.³ Excellent reviews by Yarin⁴ and Josserand and Thoroddsen⁵ cover many aspects of drop impact dynamics. In the last two decades, a number of new and surprising discoveries have been made starting with the seminal work of Xu *et al.*⁶ who showed that the pressure of the surrounding gas plays a crucial role during the splashing process. This discovery prompted Mandre *et al.*⁷ and Mani *et al.*⁸ to develop a theory to examine the role of gas and lubrication effects near the solid surface at the onset of impact. Experiments by Kolinski *et al.*,⁹ indeed, showed that a drop tends to skate on a thin layer of gas before touchdown. Another important discovery made in recent years is that drops can bounce on a smooth surface without ever making contact with it.^{10,11} A thin layer of gas cushions the impact, and lubrication pressure provides the necessary repulsion force for the drop to bounce back. Using interferometric techniques, de Ruiter

et al.^{11,12} characterized the gas film beneath the drop in great detail and showed that gas films of thickness in the micrometer and nanometer ranges are trapped beneath the drop.

In a companion paper, we recently conducted an exhaustive numerical study of a drop impacting a solid surface assuming the gas to be incompressible,¹³ and the key results of this work are briefly summarized below. Through a parametric study, the simulations revealed that wettability-independent (WI) or non-contact bouncing and wettability-dependent (WD) or bouncing with contact are separated by a transition boundary in the $We-Re$ plane. The simulations also revealed that WI bouncing is favored at low Re for a wide range of Weber numbers. In such cases, the drop spreads on a thin layer of gas beneath it. Kolinski *et al.*¹⁰ noted that large shear rates generated in this gas layer can lead to excessive dissipation, reducing the coefficient of restitution, always below 0.65 in their experiments, despite the low viscosity of air. In contrast, Richard and Quéré¹⁴ reported a coefficient of restitution close to 0.9 for a drop bouncing on a superhydrophobic surface. Such a large value in their experiments was attributed to very short contact times during

which dissipation is negligible. The results of Kolinski *et al.* are also in contrast to similar experiments by de Ruiter *et al.*¹¹ who reported a very high coefficient of restitution of 0.96 ± 0.04 . Using careful estimation of the energy budget for a wide range of We and Re , we show later that the apparent discrepancy in the coefficient of restitution between the works of Kolinski *et al.*¹⁰ and de Ruiter *et al.*¹⁵ can be resolved by examining the role of Weber and Reynolds numbers. To determine the coefficient of restitution (r_c) accurately, it is necessary to precisely compute the energy budget of a drop during a bouncing event. Closely connected to r_c is the contact time, τ , which is defined as the duration for which the drop stays in contact with the solid surface.

For water drops of about 1 mm at moderate impact velocities, typically in the range of 0.2 m/s–2 m/s, Richard *et al.*¹⁶ showed that contact time scales with the radius of the drop as $\tau \sim R^{3/2}$, obtained by balancing inertia of the drop with surface tension, and is independent of velocity. Okumura *et al.*¹⁷ showed that drop deformation and contact time depend on a delicate balance of inertia, gravity, and surface tension. At lower impact velocities, they showed that the contact time increases with a decrease in the velocity and drop deformation scales as $We^{1/2}$. A more sophisticated quasi-static model of drop impact was developed by Moláček and Bush¹⁸ who showed that the contact time and coefficient of restitution depend on both the Weber and Ohnesorge numbers.

Understanding the energetics of drop impact also helps in determining the radial extent of drop spreading upon impact. Kim and Chun¹⁹ performed experiments using a variety of drop and solid combinations to study spreading and recoiling dynamics. They used an empirically determined dissipation factor to account for viscous dissipation during drop spreading and found that an increase in the Weber number promotes faster recoil. Not surprisingly, drops with a large equilibrium contact angle were found to have very short contact times, a result consistent with the finding of Richard and Quéré.¹⁴ For drops bouncing on superhydrophobic surfaces at higher Weber numbers, contact dissipation may be small, but such drops undergo pronounced oscillations after lift-off, which generates vigorous motion inside the drop leading to additional viscous dissipation. Richard *et al.*¹⁶ argued that in their experiments, bulk of the dissipation is due to the internal motion inside the drop caused by damped surface oscillations after lift-off. We later quantify such internal dissipation in relation to surface oscillations as a function of Weber and Reynolds numbers. Pasandideh-Fard *et al.*²⁰ developed a simple model for the maximum extension diameter of the drop, D_{max} , assuming that all the initial kinetic and surface energies are converted to surface energy and viscous dissipation when the drop spreads to its maximum extent. Their model improves upon an earlier model of Chandra and Avedisian,²¹ which overestimated the value of D_{max} . Clanet *et al.*²² performed experiments with a low-viscosity drop impacting a superhydrophobic surface for moderate values of the Weber number ($2 < We < 900$), where $We = \rho_l V_0^2 R_0 / \sigma$ is the Weber number associated with the impact velocity $V_0 (= \sqrt{2gH_0})$ for a drop of radius R_0 with density and surface tension denoted by ρ_l and σ , respectively, and showed that $D_{max} \sim We^{1/4}$. This differs from the low Weber number experiments for drops on superhydrophobic surfaces where a different scaling is observed, $D_{max} \sim We^{1/2}$.

In this study, we use direct numerical simulations to calculate the energy budget of an impacting drop with emphasis on how

various exchanges of energies differ as a function of Weber and Reynolds numbers. We further show how the coefficient of restitution varies with We and Re , which will help resolve the discrepancy between the values reported by de Ruiter *et al.*¹¹ and Kolinski *et al.*¹⁰

II. NUMERICAL SETUP AND ENERGETICS

We numerically simulate a falling drop using the open source code *Gerris* in an axisymmetric configuration. The code, developed by Popinet,²³ uses an advanced quadtree adaptive mesh refinement and is well known for its accurate interface capture algorithm and surface tension implementation.²⁴ The geometry used in the current study is identical to a recently completed study for drop impact on a solid surface.¹³ For suitability of the solver to drop impact dynamics and validation studies, the reader is referred to our companion paper.¹³

A drop of radius R_0 is released from an initial height H_0 , and a schematic of the problem setup is shown in Fig. 1. The viscosity ratio between the drop and the surrounding gas is fixed at $\mu_l/\mu_g = 55.5$, mimicking a water drop falling in air. For numerical stability, we keep the density ratio fixed at $\rho_l/\rho_g = 100$ although a value of 1000 showed no appreciable difference in the results. Furthermore, since the focus will be on collision dynamics near the solid surface, the viscosity ratio plays a more important role than the density ratio. To facilitate complete rebound, the contact angle is kept fixed at 170° , inspired by the experiments of Richard and Quéré.¹⁴ For low We and Re , a drop bounces without ever making contact with the solid surface. In such cases, the impact is cushioned by a thin film of gas beneath the drop and is referred to as wettability-independent bouncing. In the work of Sharma and Dixit,¹³ we show that the drop

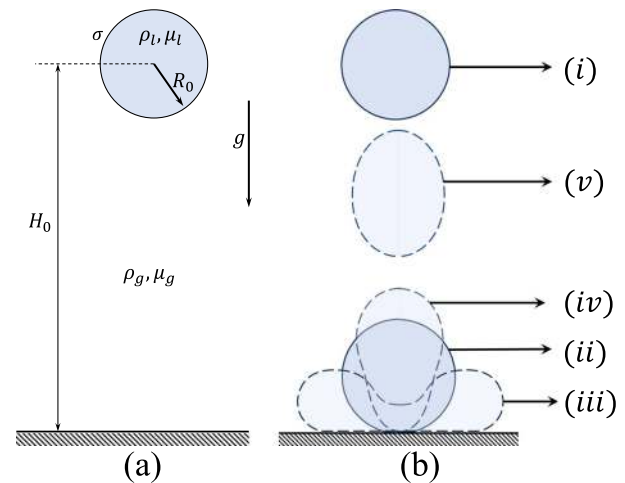


FIG. 1. (a) Schematic of the problem setup showing all the relevant parameters in the problem. (b) Schematic view of the typical shapes assumed by the drop during one complete bouncing cycle. The solid curves (i) and (ii) show the shape of the drop at $t = 0$ and at the onset of impact. The other shapes shown with dashed lines at (iii)–(v) correspond to the shape at the maximum deformation on the surface, at the instant of lift-off from the surface, and at the maximum height after impact, respectively.

shapes and the drop–gas interface profiles during contact are in good agreement with experiments for water in air scenario. Moreover, the numerical results were found to be in excellent agreement with well-established scaling laws for the height of the drop when it undergoes its first deformation before impact, $H_d \sim Ca_g^{1/2}$ derived by Pack *et al.*,²⁵ and the minimum thickness of the gas film, $h_{min} \sim St^{-8/9} We^{-2/3}$ derived by Mandre *et al.*,⁷ where $St = \rho_l V_0 R_0 / \mu_g$ is the Stokes number. A phase diagram in the We – Re plane, shown in Fig. 2, shows two distinct regimes of impact referred to as wettability-independent (WI) contact and wettability-dependent (WD) contact. In the WI regime, the drop is supported on a thin gas layer whose thickness scales with We and St . In the WD regime, contact occurs either at the outer periphery of the drop or near the axis of symmetry. To enable complete rebound, all our simulations are carried out at a fixed contact angle of 170° , representing bouncing from superhydrophobic surfaces similar to the experiments of Richard and Quéré.¹⁴

The primary goal of this study is to obtain a detailed energy budget as the drop completes one bouncing cycle, i.e., a drop from an initial release height H_0 impacts the surface and reaches a new height after lift-off, H_1 . During this motion, potential energy of the drop, $E_p(t)$, converts to kinetic and surface energies, $E_K(t)$ and $E_S(t)$. Drag due to the surrounding gas and internal motions within the drop contributes to viscous dissipation. Let E_0 be the initial energy of the drop, given by $E_0 = E_p^{(0)} + E_S^{(0)}$. Applying the principle of energy conservation, the drop has to obey the following relation:

$$E_p(t) + E_K(t) + E_S(t) + D(t) = E_0, \quad (1)$$

where $D(t)$ represents viscous dissipation of energy. It is instructive to combine energies associated only with the drop to highlight the role played by the gas. We therefore define

$$E(t) = E_p(t) + E_{K,d}(t) + E_S(t), \quad (2)$$

where the subscript d in the kinetic energy shows that this energy is only associated with the drop motion. All the energies defined

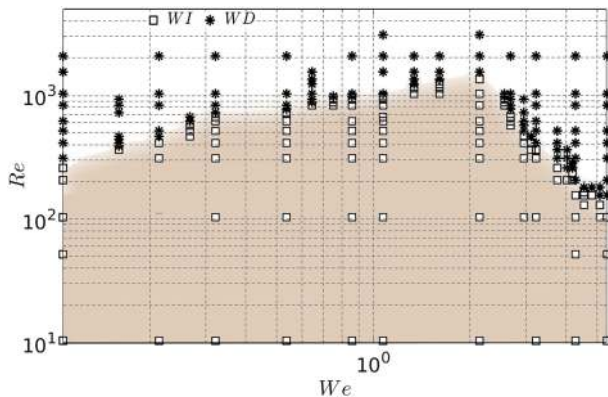


FIG. 2. Phase diagram in the Re – We plane showing two distinct regimes, the wettability-independent regime (WI) (shown with a shaded region) and the wettability-dependent regime (WD). The symbols correspond to parameter values where simulations are carried out for one complete bouncing cycle. The transition between the two regimes is grid dependent (see the companion paper¹³ for more details).

above can be calculated in terms of the flow fields and drop shape numerically using the integrals

$$E_p(t) = \int_{\Omega} \rho_l B g h d\Omega, \quad (3)$$

$$E_{K,d}(t) = \frac{1}{2} \int_{\Omega_d} \rho_l (u^2 + v^2) d\Omega = \frac{1}{2} \int_{\Omega} \rho_l B (u^2 + v^2) d\Omega, \quad (4)$$

$$E_{K,g}(t) = \frac{1}{2} \int_{\Omega_g} \rho_g (u^2 + v^2) d\Omega = \frac{1}{2} \int_{\Omega} \rho_g (1-B) (u^2 + v^2) d\Omega. \quad (5)$$

In the above expressions, u and v are radial and axial velocities, and B is the volume fraction of liquid with $B = 1$ representing the liquid phase and $B = 0$ representing the gas phase. In the volume-of-fluid method adopted in the current study, the interface cells have a value of B between 0 and 1 such that the density of any cell is given by $\rho = B\rho_l + (1 - B)\rho_g$. When the drop is not in contact with the solid surface, surface energy is simply the product of surface tension (liquid–gas free energy, σ) and surface area of the drop. However, when the drop is in contact with the solid, additional interfacial energy between the drop and the solid, σ_{sl} , needs to be taken into account. For a contact angle, $\theta = \theta_e$, and using Young’s law, the surface energy can be defined as

$$E_S(t) = \begin{cases} \sigma A_s(t), & \text{during flight} \\ \sigma(A_s(t) - a_s(t) \cos(\theta_e)), & \text{during contact,} \end{cases} \quad (6)$$

where σ is the surface tension of the drop–gas interface, $A_s(t)$ is the surface area of the drop–gas interface, and $a_s(t)$ is the surface area of the drop–solid interface.

Energy lost through viscous dissipation in Eq. (1) is obtained by integrating the rate of dissipation of mechanical energy, per unit mass of the fluid, due to viscosity, Φ , as

$$D(t) = \int_0^t \Phi(s) ds, \quad (7)$$

where $\Phi(t)$ can be written in terms of the stress tensor \mathbf{T} and rate-of-strain tensor \mathbf{S} as

$$\begin{aligned} \Phi &= \int_{\Omega_d \cup \Omega_g} \mathbf{T} : \mathbf{S} d\Omega \\ &= \int_{\Omega} \left[2\mu \left(\left(\frac{\partial u}{\partial r} \right)^2 + \left(\frac{\partial v}{\partial y} \right)^2 + \left(\frac{u}{r} \right)^2 \right) + \mu \left(\frac{\partial v}{\partial r} + \frac{\partial u}{\partial y} \right)^2 \right] d\Omega. \end{aligned} \quad (8)$$

Here, Ω_d and Ω_g represent the drop and gas phases, respectively, and $\mu = B\mu_l + (1 - B)\mu_g$ is the average viscosity in a cell. Since some of the drop’s energy is lost to the kinetic energy of the gas, $E_{K,g}$, we define two new energy terms,

$$E_D(t) = E(t) + D(t), \quad (9)$$

$$E_T(t) = E_D(t) + E_{K,g}(t). \quad (10)$$

The first expression, $E_D(t)$, represents the total energy of the drop including viscous dissipation (in drop and gas), while the second expression, $E_T(t)$, is the total energy of the system accounting for all losses; thus, E_T should be equal to E_0 at all times. Apart from minor numerical errors, E_T is practically indistinguishable from E_0 in our simulations, guaranteeing the numerical accuracy of the solver.

TABLE I. Glossary of important parameters used in the study.

Initial energy of the drop ($t = 0$)	$E_0 = E_P(t) + E_K(t) + E_S(t) + D(t)$	Equation (1)
Total energy of the drop	$E(t) = E_P(t) + E_{K,d}(t) + E_S(t)$	Equation (2)
Potential energy of the drop	$E_P(t)$	Equation (3)
Kinetic energy of the drop	$E_{K,d}(t)$	Equation (4)
Kinetic energy of the gas	$E_{K,g}(t)$	Equation (5)
Surface energy of the drop–gas interface	$E_S(t)$	Equation (6)
Viscous dissipation	$D(t)$	Equation (7)
Total energy loss	$L_T(t)$	Equation (11)
Energy loss in contact	$L_c(t)$	Equation (12)
Coefficient of restitution	$r_c = \sqrt{ V_1 / V_0 }$	Equation (14)
Reynolds number	Re	$\frac{\rho_l V_0 R_0}{\mu_l}$
Stokes number	St	$\frac{\mu_l}{\rho_l V_0 R_0}$
Weber number	We	$\frac{\mu_g}{\rho_l V_0^2 R_0}$
		σ

Having defined all the relevant energy quantities, we define two new quantities to quantify energy loss during drop impact. The total energy loss during one complete bouncing cycle for a drop starting at height H_0 until it again attains a new maximum height H_1 after its first impact can be calculated in terms of the total loss, L_T , defined by

$$L_T = E_0 - E_1. \quad (11)$$

Similarly, loss of energy during impact can be calculated as

$$L_c = E_b - E_a, \quad (12)$$

where E_b and E_a are the total energies of the drop before (taken to be the instant of time at when the drop undergoes its first deformation) and after impact, respectively. Table I summarizes all the energies and parameters used in this work.

III. RESULTS AND DISCUSSION

A. Energy budget

All energies are non-dimensionalized by the initial total energy, E_0 , and their variation with time is shown in Fig. 3 as the drop

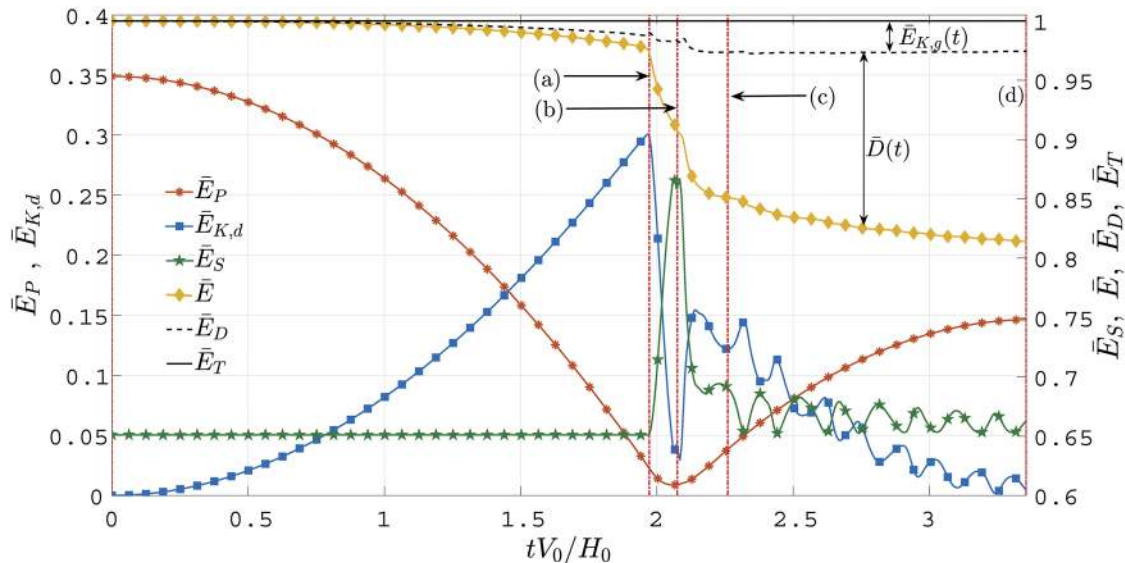


FIG. 3. Energy budget for one complete bouncing cycle for $We = 3.21$ and $Re = 207$ showing various energies associated with the drop and the gas non-dimensionalized with the initial energy E_0 . The kinetic, $\bar{E}_{K,d}$, and potential energies, \bar{E}_P , are shown on the left y axis, while surface energy, \bar{E}_S , energy of the drop without viscous dissipation, \bar{E} , energy of the drop with viscous dissipation, \bar{E}_D , and total energy of the drop and gas, \bar{E}_T , are shown on the right y axis. See text for more details. Note the difference in the scale on both the left and right y axes. The vertical dashed-dotted lines marked (a)–(d) represent the time at the onset of impact, at the maximum deformation of the drop, at the onset of lift-off, and at the maximum height, respectively.

completes one complete rebound cycle for $We = 3.21$ and $Re = 207$, a case in the wettability-independent regime of Fig. 2. Variations in energy budget are punctuated by distinct phases in drop's evolution during the impact process, which are shown by vertical lines marked (a)–(d). The corresponding drop shapes at each of these times are shown in Fig. 4. At $t = 0$, the drop descends from rest possessing only potential and surface energies. The ratio of these two energies is given by

$$\frac{E_p^{(0)}}{E_s^{(0)}} = \frac{We}{6}. \tag{13}$$

In this particular case, $E_s^{(0)} > E_p^{(0)}$ due to the small Weber number used. At the instant shown by (a) in Fig. 3, the drop begins to deform from its spherical shape indicated by a concomitant increase in the surface energy. At this instant of time, the kinetic energy of the drop is at its maximum, and the drop shape is shown in Fig. 4(a). A region of high pressure is developed beneath the drop, which rapidly decelerates the drop's motion. The drop soon makes “touchdown” but, in this case, is supported on a thin cushion of gas below it. The kinetic energy of the drop then rapidly reduces at the expense of its surface energy, and the drop deforms to its maximum radial extent at the time shown by (b). The drop shape along with the pressure field inside it at this time is shown in Fig. 4(b). Even at the drop's maximum extent, internal circulation does not completely cease, giving rise to a non-zero kinetic energy. In the work of Sharma and Dixit,¹³ we show that the maximum spreading diameter obeys the scaling, $D_{max} \sim We^{1/2}$. This scaling was first derived by Richard and Quéré¹⁴ using the argument of exchange of kinetic and surface energies during impact, and the results in Fig. 3 are consistent with their findings. Surface tension then causes the drop to retract, and it eventually achieves lift-off from the solid surface at time (c). The drop takes the shape of a distorted prolate spheroid, as shown in Fig. 4(c). Most of the viscous dissipation occurs during impact as evident from a large decrease in drop's energy, $E(t)$, given in Eq. (2), between times (a) and (c). The drop continues to oscillate during its ballistic motion, causing additional viscous dissipation due to internal circulation inside the drop. As a result, both the kinetic and surface

energies exhibit damped oscillations, providing a route for continuous loss of drop's energy during its flight. In Sec. IV, we return to the issue of energy loss and compare loss during contact and during flight in greater detail. It has to be noted that only a small fraction of the drop's energy is exchanged with the gas, shown as $E_{K,g}$, in this case, less than 2.5%. During drop's upward motion, we observe a nearly perfect exchange of kinetic and surface energies, as shown in Fig. 5. To compare these energies, we plot only the fluctuating part of the energies obtained by subtracting out the moving-average value. The drop eventually reaches a new maxima, H_1 , losing ~20% of its total energy E_0 , and the drop shape at the new height is shown in Fig. 4(d).

We now examine how the energy budget for a falling drop changes with time for a sample case in the wettability-dependent regime of the phase diagram of Fig. 2. The energy budget with $We = 3.21$ and $Re = 1035$ is shown in Fig. 6 and has to be viewed in conjunction with the evolution of drop shapes shown in Fig. 7 and three-dimensional and streamline plots showing the bubble capture and escape process in Figs. 8–10, respectively. The evolution of all energies until the first deformation of the drop, shown with the vertical dashed-dotted line at (a), is identical to the previous case at $Re = 207$. Inertia causes the drop to rapidly spread on the surface until time (b) when the surface energy reaches a maximum at the expense of kinetic energy. The interface at the axis of symmetry continues to move downward, while the drop retreats inward radially. Capillary waves generated near the surface travel azimuthally along the drop's surface amplifying in the process. These waves focus at the axis of symmetry, resulting in vigorous vertical oscillations of the upper interface of the drop, as shown in Fig. 8(a). The interface then descends downward and undergoes necking. This process traps a gas bubble inside it, as shown in Fig. 8(d). Cusp-like regions are formed at the axis of symmetry that results in localized regions of high pressure, Fig. 7(c). Fluid rapidly moves away from this high pressure zones, resulting in the formation of a high speed jet. On the upper side, the high speed jet breaks down into tiny drops due to rapid acceleration, whereas on the lower side, this jet can collide with the trapped bubble, generating tiny secondary bubbles inside the bubble (see movie-1 of the supplementary material). The intense motion results in some of the drop's energy to be lost to accelerate the gas,

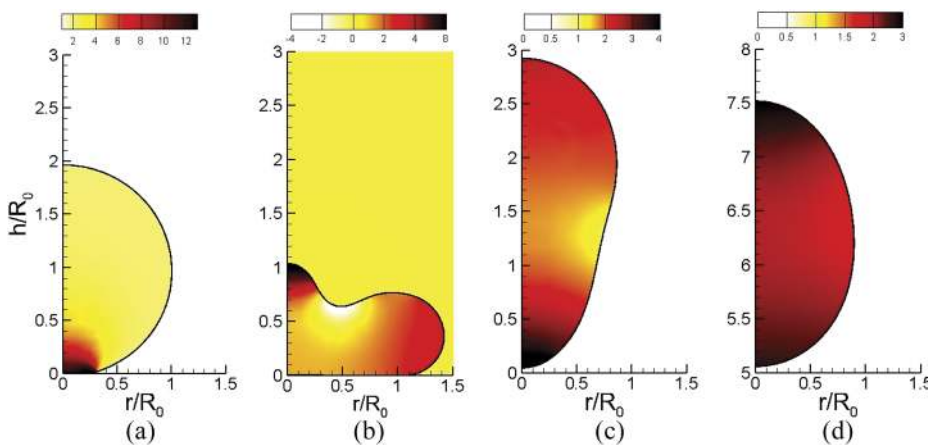


FIG. 4. Drop shapes for $We = 3.21$ and $Re = 207$ at four different times: (a) $\bar{t} = 1.9719$, (b) $\bar{t} = 2.075$, (c) $\bar{t} = 2.26$, and (d) $\bar{t} = 3.349$. The color contours show the variation of non-dimensional pressure, $\bar{P} = P/(\sigma/R_0)$. The four panels correspond to time instants shown with the vertical dashed-dotted lines in the energy budget of Fig. 3. Note that contour levels are different in the four panels.

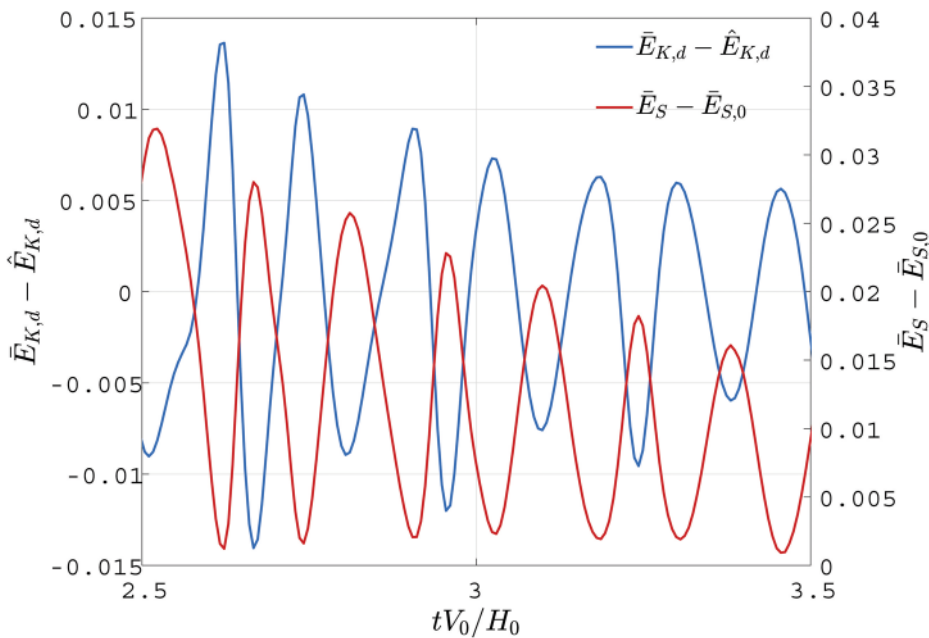


FIG. 5. A close-up view of the fluctuating part of the kinetic and surface energies of the drop after rebound, from Fig. 3, showing perfect exchange of energies between the two. $\hat{E}_{K,d}$ represents the moving-average value of the kinetic energy, and $\bar{E}_{S,0}$ is the initial surface energy of the drop.

some to viscous dissipation due to rapid and vigorous motions inside the drop, and a small portion to the mass lost from ejection of tiny droplets. This process occurs over a very short timescale, shown at time (c), and causes a sudden drop in the drop’s energy, shown as $\Delta\bar{E}_{bub,F}$, which represents the energy lost during bubble entrapment. We show later that bubble entrapment and escape result in a sudden increase in viscous dissipation. Figure 9 shows the sequence of events leading to trapping of the bubble. Large scale inward motion of the drop, as shown in Figs. 9(a)–9(c), shows trapping of a gas bubble inside the drop. Strong vortical flow is generated inside the bubble as revealed in close-up views shown in Figs. 9(e) and 9(f), consistent with the findings of Tripathi *et al.*²⁶ who noted that

vorticity tends to concentrate in the lighter fluid. At the end of the bubble entrapment process, the upper interface of the drop tends to violently recoil, releasing a high speed jet. Contours of velocity magnitude in Fig. 9 reveal that significantly high velocities are generated in the gas phase, particularly after the complete enclosure of the bubble inside the drop. In physical terms, consider a 1 mm water drop impacting a surface with the same We , as given in Fig. 9. This translates to impact speed, $V_0 \approx 0.46$ m/s, which leads to a gas velocity of about 46 m/s.

The trapped bubble remains lodged inside the drop during lift-off at time (d) in Fig. 6 and also shown in Fig. 7(d), and in some cases, it even stays inside the drop until the drop undergoes its

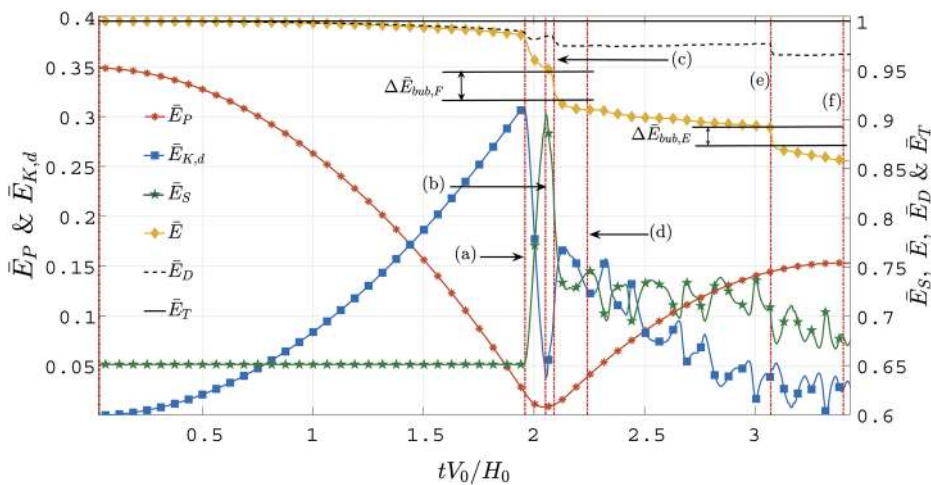


FIG. 6. Energy budget for one complete bouncing cycle for $We = 3.21$ and $Re = 1035$ showing various energies associated with the drop and the gas non-dimensionalized with the initial energy E_0 . All quantities are the same, as defined in Fig. 3. The vertical dashed-dotted lines marked (a)–(f) represent the times at the onset of impact, at the maximum deformation of the drop, at the instant of bubble entrapment, at the onset of lift-off, at the instant of bubble escape, and at the maximum height after impact, respectively.

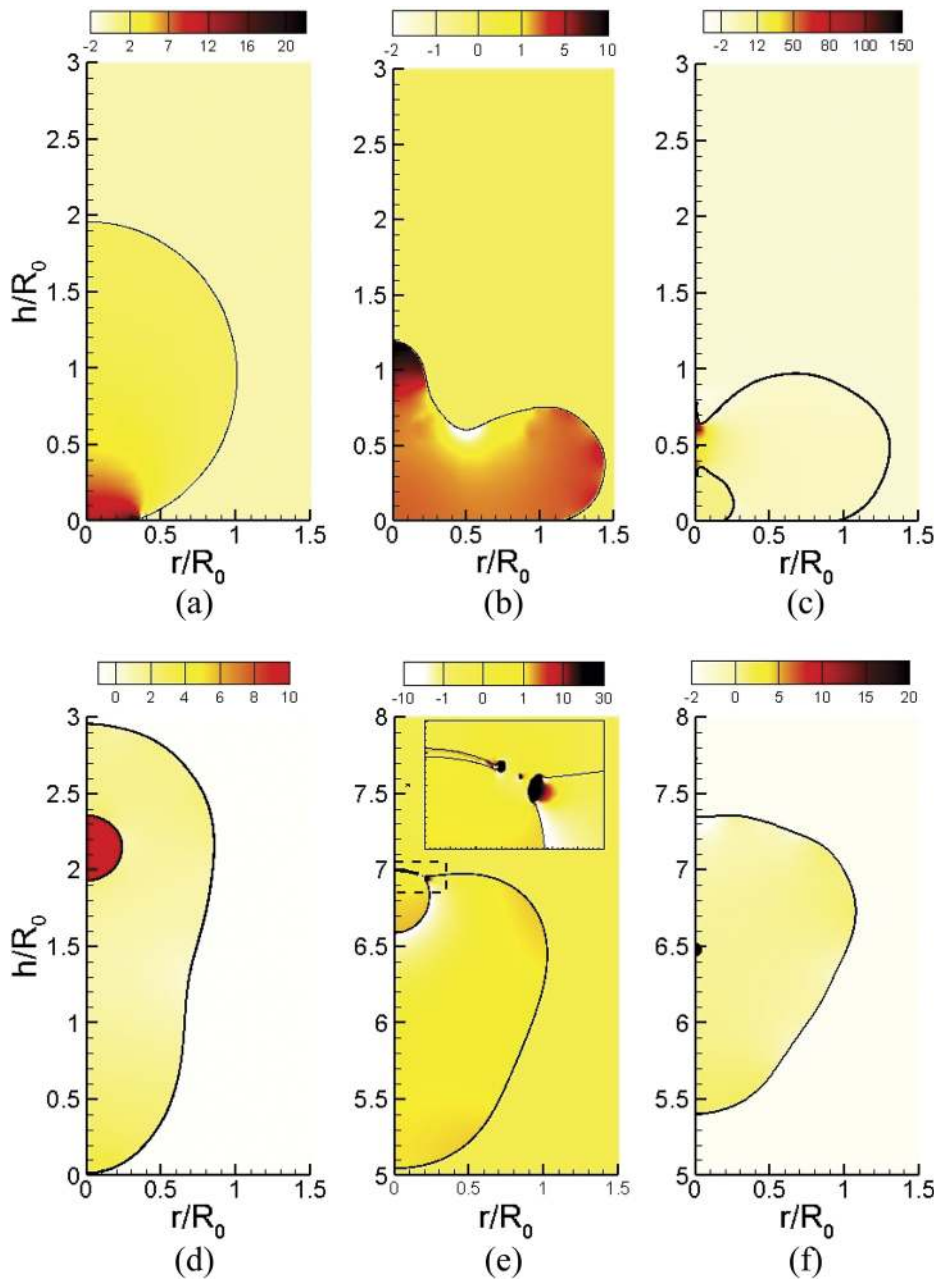


FIG. 7. Drop shapes for $We = 3.21$ and $Re = 1035$ at six different times: (a) $\bar{t} = 1.959$, (b) $\bar{t} = 2.047$, (c) $\bar{t} = 2.09$, (d) $\bar{t} = 2.241$, (e) $\bar{t} = 3.071$, and (f) $\bar{t} = 3.374$. The color contours show the variation of non-dimensional pressure, $\bar{P} = P/(\sigma/R_0)$. The six panels correspond to the time instants shown with the vertical dashed-dotted lines in the energy budget of Fig. 6. Note that contour levels are different across the panels. See the [supplementary material](#) for a three-dimensional evolution of bubble entrapment and escape.

second bounce. In this particular case, the trapped bubble slowly drifts upward and eventually emerges out of the drop in a violent escape at time (e). During its emergence, the bubble traps a thin curved film of liquid between its upper surface and the drop's surface. This thin film ruptures at its periphery, as shown in Fig. 7(e), similar to the process described by Manica *et al.*²⁷ Very large pressures are generated at the tip of the filament due to tiny curvatures there [see the inset of Fig. 7(e)]. This causes the tip to rapidly retract allowing pressurized gas inside the bubble to rapidly escape, imparting kinetic energy to the gas. Figure 10 shows the bubble

escape process in finer detail. A thin film of liquid is trapped between the upper surface of the drop and the escaping bubble, as shown in Fig. 10(a). As soon as the rupture is initiated, pressurized gas inside the bubble rapidly escapes, as evident from the contours of velocity magnitude shown in Figs. 10(b) and 10(c). Simultaneously, the thin liquid film shown in Fig. 10(d), now in the form of a filament, rapidly retreats radially in a time of approximately $\Delta \bar{t} \approx 8 \times 10^{-4}$. In dimensional terms, this amounts to a time of about $30 \mu\text{s}$. A counter-rotating toroidal vortex pair, Fig. 10(e), is generated in the gas generating a great deal of viscous dissipation. The retracting

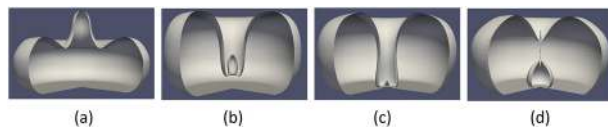


FIG. 8. Three-dimensional representation of drop shapes showing the process of bubble entrapment during drop impact. The four panels are in sequence (from left to right) at non-dimensional time $\bar{t} = (t - t_0)/\tau$: (a) 0.82 at maximum spreading, (b) 1.01 at the intermediate stage of downward motion of the upper interface, (c) 1.06 at the onset of necking of the cylindrical filament, and (d) 1.12, high speed jet ejection at the axis of symmetry, where t_0 is the time of first deformation. Parameters used are $We = 3.21$ and $Re = 1035$. See the [supplementary material](#) for a three-dimensional evolution of bubble entrapment.

filament collapses upon itself, resulting in a vertically accelerating jet [Fig. 10(f)], which can hit the drop during its rebound and entrap tiny gas bubbles again. These tiny secondary bubbles, as shown in Fig. 7(f), may again create tertiary bubbles, but our simulations do not have sufficient resolution to track escape of these bubbles. See movie-2 of the [supplementary material](#) for a 3D visualization of an escaping bubble. The process of bubble escape causes a sudden drop in the drop's total energy, $\Delta E_{bub,E}$, as shown at time (e) of Fig. 6, where the subscript E denotes an escaping bubble.

B. Coefficient of restitution

In the above discussion, energy budgets were presented for two specific parameter values, viz., $Re = 207$, $We = 3.21$ and $Re = 1035$, $We = 3.21$. A number of interesting facts emerged from this analysis, which are briefly listed as follows: (i) energy loss occurs when the drop is in contact with the solid surface, and (ii) energy loss occurs when the drop is in motion after bouncing from the surface. The former occurs primarily due to large shear stresses generated near the solid surface, in both the gas and the drop, while the latter occurs due to surface oscillation-induced internal motions inside the drop, which generates additional viscous dissipation. We estimate both

these energy losses for the entire range of We and Re shown in the phase diagram of Fig. 2. Conventionally, energy loss during impact is represented through the coefficient of restitution, defined as

$$r_c = \frac{|V_1|}{|V_0|}, \quad (14)$$

where V_1 is the velocity after impact and V_0 is the velocity of the drop before impact. In the case of a drop undergoing large shape changes, determination of the velocity is often difficult in experiments. In such cases, a height-based coefficient of restitution has sometimes been used,

$$r_h = \sqrt{\frac{H_1}{H_0}}, \quad (15)$$

where H_1 is the maximum height attained by the drop after the impact and H_0 is the initial release height at $t = 0$.

The two definitions of the restitution coefficient will be the same if viscous dissipation in the drop during its ballistic motion before and after impact as well as drag from the surrounding gas are negligible.

de Ruiter *et al.*¹⁵ reported a coefficient of restitution, $r_c \geq 0.88$, and, in some cases, reported values as high as 0.96 ± 0.04 . This value is in contrast to the value reported by Kolinski *et al.*¹⁰ who reported $r_h \leq 0.65$ based on a height-based measurement, and it was suggested that such low values in r_h are due to the formation of a strong shear layer in the gas cushion beneath the drop. de Ruiter *et al.*¹⁵ used water drops in their experiments, whereas Kolinski *et al.*¹⁰ used water-glycerol mixtures, which increases the viscosity of the drops. Furthermore, the impact velocities are lower in the latter case, which results in lower Re values. In both the studies, the surfaces are hydrophilic, and the drops never make physical contact with the solid surface for the entire range of Re and We considered in the present study. The large variation in the value of the restitution coefficient in the two studies can be reconciled by examining the role of Re and We in these experiments. High values of r_c were also reported in the works of Footte²⁸ and Richard and Qu  r  ,¹⁴ the

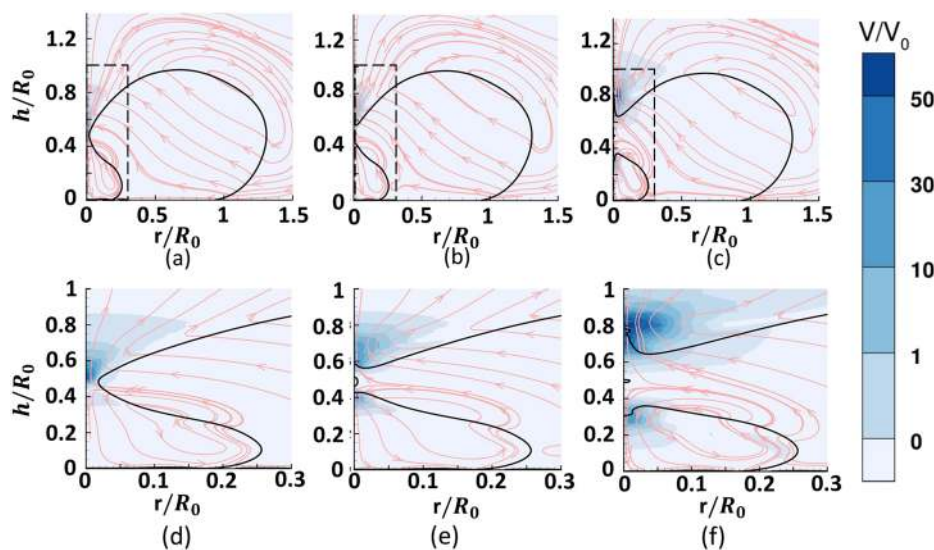


FIG. 9. Flow field during the bubble entrapment process for $We = 3.21$ and $Re = 1035$ showing instantaneous streamlines and contours of velocity magnitude at (a) $\bar{t} = 2.0902$, (b) $\bar{t} = 2.0904$, and (c) $\bar{t} = 2.0908$. Close-up views shown in panels (d)–(f) shows the vortical motion inside the trapped bubble. The high speed jet generates intense velocities near the axis of symmetry imparting kinetic energy to the gas and also causes viscous dissipation during bubble entrapment. See the [supplementary material](#) for a three-dimensional evolution of bubble entrapment.

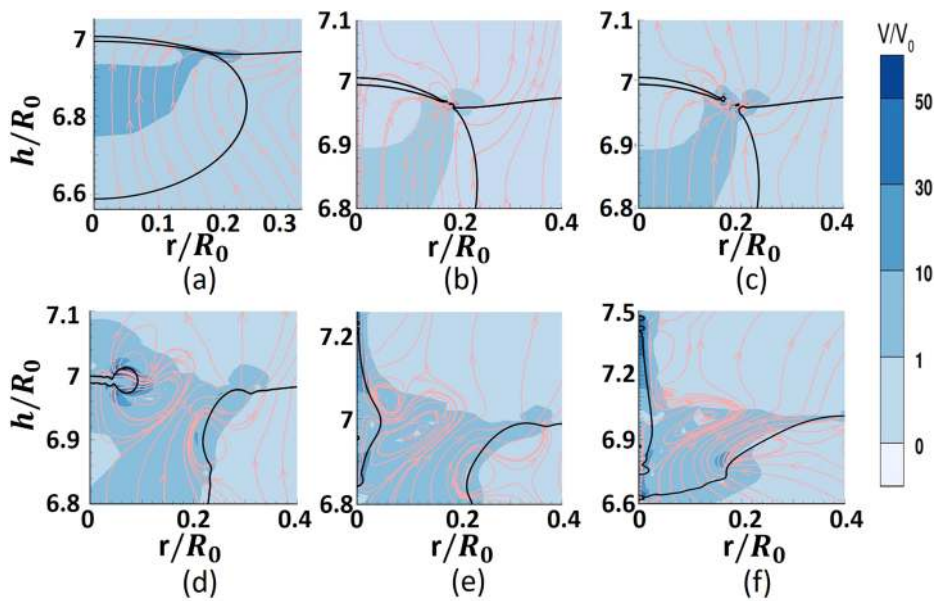


FIG. 10. A close-up view of the fluid motion generated during escape of the entrapped bubble. A thin liquid film trapped between the escaping bubble and the upper surface of the drop ruptures [(a) and (b)] and rapidly retreats [(c) and (d)]. This generates another high speed jet at the axis of symmetry [(e) and (f)]. The panels are shown in sequence at non-dimensional times, \tilde{t} : (a) 3.0705, (b) 3.071, (c) 3.0711, (d) 3.0718, (e) 3.0724, and (f) 3.0737. See the [supplementary material](#) for a three-dimensional evolution of bubble escape.

former being a numerical study for head-on collision of two drops, while the latter being an experimental study of drops bouncing on superhydrophobic surfaces. de Ruiter *et al.*¹⁵ attributed such high values to the absence of the contact line and the strong repulsion force provided by a lubricating gas layer, while Richard and Quéré¹⁴ attributed high values of r_c to the low contact time in their experiments. It is possible that contact-less bouncing also occurred in the work of Richard and Quéré,¹⁴ but there is no evidence of this in their paper. Richard and Quéré¹⁴ suggested that a great deal of energy loss occurs when the drop is in flight. By calculating the kinetic energy based on the center of mass of the drop and kinetic energy due to internal motions inside the drop, de Ruiter *et al.*¹⁵ obtained a detailed energy budget of the drop. Major losses during each bounce were attributed to viscous losses in the thin lubricating gas layer. This is consistent with the reason provided by Kolinski *et al.*¹⁰ who attributed low r_c in their experiments to large dissipation in the gas layer.

The above survey suggests that viscous losses in the thin intervening gas layer varies as a function of St and We , where $St = Re/\lambda$ is the Stokes number and $\lambda = \mu_g/\mu_l$ is the viscosity ratio. To reconcile differences between the above studies, we extract the coefficient of restitution r_c from our simulation data and plot it in the $We-Re$ plane, as shown in Fig. 11. The experimental values of the restitution coefficient in the work of de Ruiter *et al.*¹⁵ and Kolinski *et al.*¹⁰ are shown with symbols, while the simulation values at the same Re and We are shown alongside in brackets. It is clear that the agreement with simulations and experiments is satisfactory. More importantly, our simulations reveal that the restitution coefficient strongly varies with both Re and We . The differences observed in the two sets of experiments can thus be attributed to very different experimental parameters used in the two studies. Figure 11 also reveals that for $We \gtrsim 1$, r_c becomes less sensitive to the Reynolds number and rapidly decreases with an increase in We . At higher We , the drop undergoes large scale deformation, generating a great deal of vigorous motions

inside the drop. This motion coupled with lower values of surface tension at higher We causes the drop to spread to greater extent on the solid surface obeying the scaling law $r_k \sim We^{1/4}$, where r_k is the radial extent of the gas layer (see the work of Sharma and Dixit¹³). This generates a strong shear in the gas layer, generating excess dissipation at the location of h_{min} , i.e., where the gas layer is at its thinnest. This can be easily verified by determining the non-dimensional rate of dissipation written as Φ/Φ^* , where Φ is given by Eq. (8) and Φ^* is the characteristic value of dissipation. Using impact velocity V_0 and gas layer thickness when the drop undergoes its first deformation, $H_d \sim R_0 Ca_g^{1/2}$,¹³ we have $\Phi^* = V_0 \sigma / \lambda R_0^2$. Contours of Φ/Φ^* shown in Fig. 12 at two different times show that dissipation, indeed, assumes large values in the thin gas film, both during the spreading and receding stages. Low values of dissipation are found inside the drop consistent with the observation by Gopinath and Koch²⁹ who noted that for $Re \gg We^{1/2}$, viscous dissipation inside the drop can be neglected.

At lower We , Fig. 11 shows that r_c strongly depends on the value of Re at lower Reynolds numbers and weakly depends on the Weber number. This is a direct consequence of increased viscosity at lower Re , which causes large dissipation in the gas film. At low We , the deformation of the drop is also reduced; thus, r_c values remain relatively high in this region for a wide range of Reynolds numbers, as shown in Fig. 11. The role of We and Re becomes even more evident in Fig. 13 where non-dimensional viscous dissipation, $\bar{D} = D/E_0$, is plotted for four different parameter combinations. This can be explained using the simple analogy of a mass-spring-damper system, given by

$$m\ddot{y} + \gamma(We, Re)\dot{y} + k(We)y = F(t), \quad (16)$$

where damping coefficient γ is a function of both Re and We , whereas stiffness k is a function of We alone. For very low We , surface tension dominates over inertia, and the drop does not exhibit large scale oscillations on its surface. In this limit, the drop largely

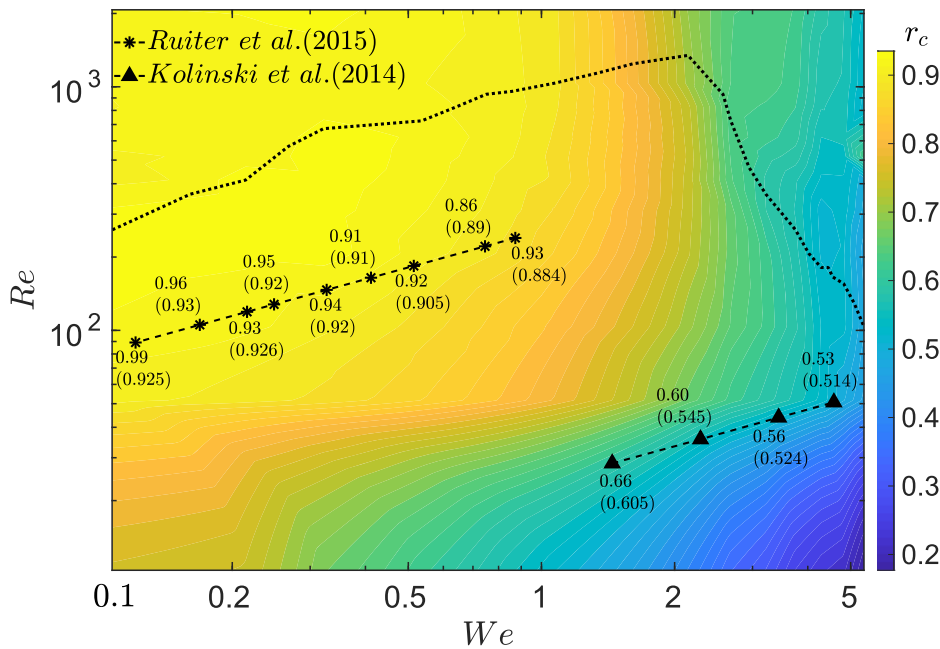


FIG. 11. Variation of the coefficient of restitution, r_c , on the We - Re plane. The experimental values obtained by de Ruiter *et al.*¹⁵ (water droplet impact on glass) and Kolinski *et al.*¹⁰ (water-glycerol drop on mica) are shown along with the simulation given in brackets. Simulation values are within 10% of the experimentally obtained values.

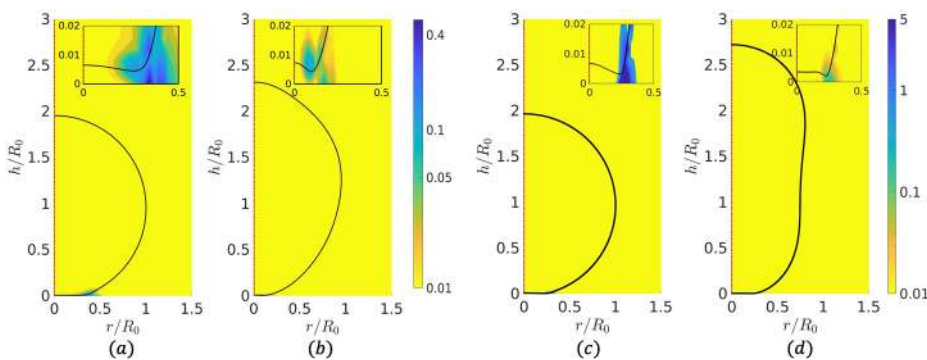


FIG. 12. Contours of the non-dimensional rate of dissipation (Φ/Φ^*) during spreading and receding stages of the drop for $We = 1.07$ and $Re = 207$ at (a) $\hat{t} = 0.19$ and (b) $\hat{t} = 2.372$. The inset shows the drop-gas interface profile near the solid surface where the rate of dissipation is maximum.

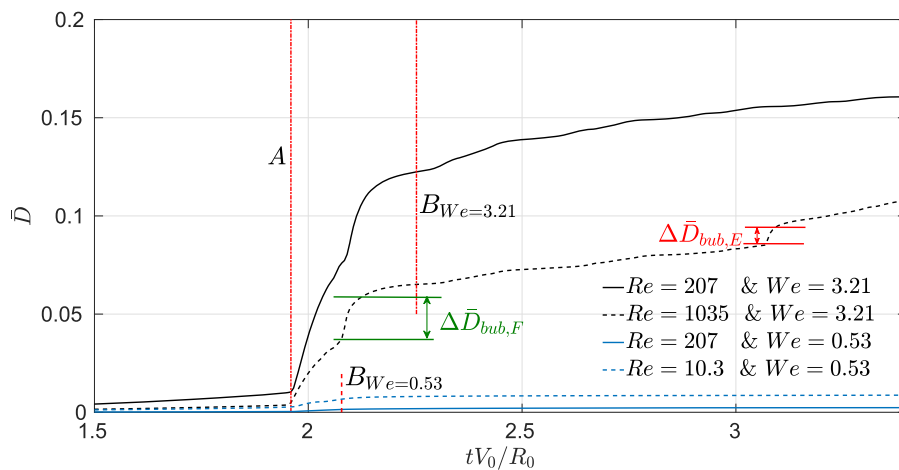


FIG. 13. Variation of non-dimensional viscous dissipation, $\bar{D} = D/E_0$, for four combinations of Re and We . The vertical dashed-dotted and dashed lines, common for the same value of We , show the time instant when contact begins (shown as A) and when the drop departs the surface (shown as B).

remains spherical, and dissipation/damping simplifies to $\gamma \approx \gamma(Re)$. However, at higher We , large scale oscillations inside the drop induce undulations in the underlying gas layer beneath the drop.¹³ The radial extent of the gas layer is large at high We , which generates strong shear stress in the gas layer, causing viscous dissipation. Furthermore, surface oscillation induced motions contribute to additional viscous dissipation during drop motion in flight.

The effect of We and Re or St on viscous dissipation can be understood through a simple scaling law derived below. Viscous dissipation during contact given in Eq. (8) scales as

$$D \sim \mu_g \left(\frac{V}{h}\right)^2 \Omega T, \tag{17}$$

where V and h are characteristic velocity and length scales in the gas film, Ω is the volume of the gas film beneath the drop, and T is the characteristic time scale. Using impact velocity V_0 for velocity, gas thickness at the drop's first deformation, H_d , for thickness, and

inertia-capillary time scale $\tau \sim (\rho_l R_0^3 / \sigma)^{1/2}$ for time, we have

$$D \sim \mu_g \left(\frac{V_0}{H_d}\right)^2 \pi r_k^2 H_d \tau \sim \mu_g \frac{V_0^2}{H_d} r_k^2 \tau \tag{18}$$

where Ω is taken to be the volume of a uniform gas film of thickness H_d and radius r_k . In the work of Sharma and Dixit,¹³ we show that $H_d \sim R_0 Ca_g^{1/2}$, where $Ca_g = We/St$ is the capillary number based on gas viscosity and $r_k \sim R_0 We^{1/4}$. Using these expressions, viscous dissipation reduces to

$$D \sim \mu_g V_0 R_0^2 We^{1/2} St^{1/2}. \tag{19}$$

Figures 14(a) and 14(b) show variation of non-dimensional viscous dissipation with the Stokes number (at fixed We) and Weber number (at fixed St), and the agreement with the scaling law derived in Eq. (19) is excellent except for low values of We . Our scaling law derivation makes two important assumptions: (i) validity of the lubrication approximation and (ii) time scale $T \approx \tau$. At very low We , the extent of the gas film, defined as the radial location of the outer minima in gas film thickness, follows the scaling $r_k \sim R_0 We^{1/4}$. Hence, in the low We cases, lubrication approximation becomes questionable. Following the work of Moláček and Bush¹⁸ who showed that, at low We , the time of contact increases with a decrease in the Weber number, our second assumption becomes questionable at low We . These two reasons explain the deviation of our results in Fig. 14(b) from the scaling law (19).

IV. ENERGY LOSSES DURING A BOUNCING CYCLE

In Sec. III B, the coefficient of restitution was estimated based on the velocities before and after impact. Richard and Quéré¹⁴ estimated that most of the energy lost in their experiments was due to viscous dissipation during flight. This can occur owing to drag from the surrounding gas and internal motions generated inside the drop due to surface oscillations. It is also relevant to note that Kolinski *et al.*¹⁰ calculated the coefficient of restitution based on maximum drop heights given in Eq. (15). Large amplitude multi-mode drop oscillations generate large internal circulations inside the drop, which leads to viscous dissipation that cannot be accounted for in the restitution coefficient based on the change in the velocity during impact. In Fig. 15(a), we first plot the total energy loss, $L_T = E_0 - E_1$, that occurs during one complete bouncing cycle, i.e., until the centroid of the drop attains a maxima after impact. The contour of energy loss, L_T , strongly depends on We as evident from the nearly vertical contours. At large We , energy loss reaches to about 0.4, i.e., 40% of drop's energy is lost in one bouncing cycle.

To investigate whether this loss occurs during contact or during flight, we plot the ratio of energy lost during contact to total energy lost, L_c/L_T , as shown in Fig. 15(b). We are primarily interested in the wettability-independent region, which occurs below the dotted curve in Fig. 15(b). Consistent with the discussion in Sec. III B, at high We , energy lost during contact is the primary contributor for total energy loss and can be up to 80% of the total loss. At a high Weber number, which is also the region of interest in the

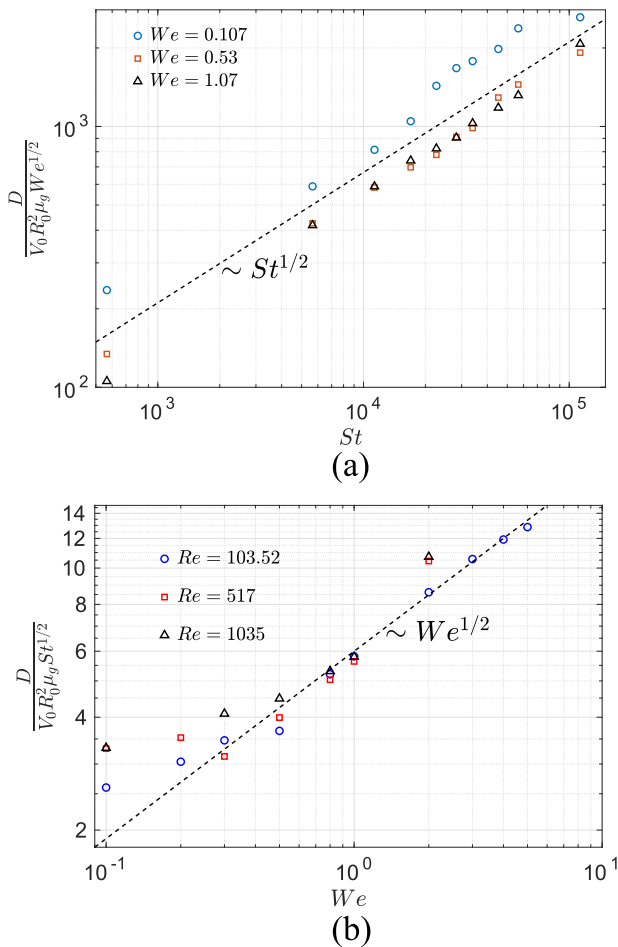


FIG. 14. Scaling for non-dimensional viscous dissipation as a function of (a) Stokes and (b) Weber numbers. The symbols in each plot correspond to three different values of Weber numbers (a) or Reynolds numbers (b). The dashed line shows the scaling law given by Eq. (19).

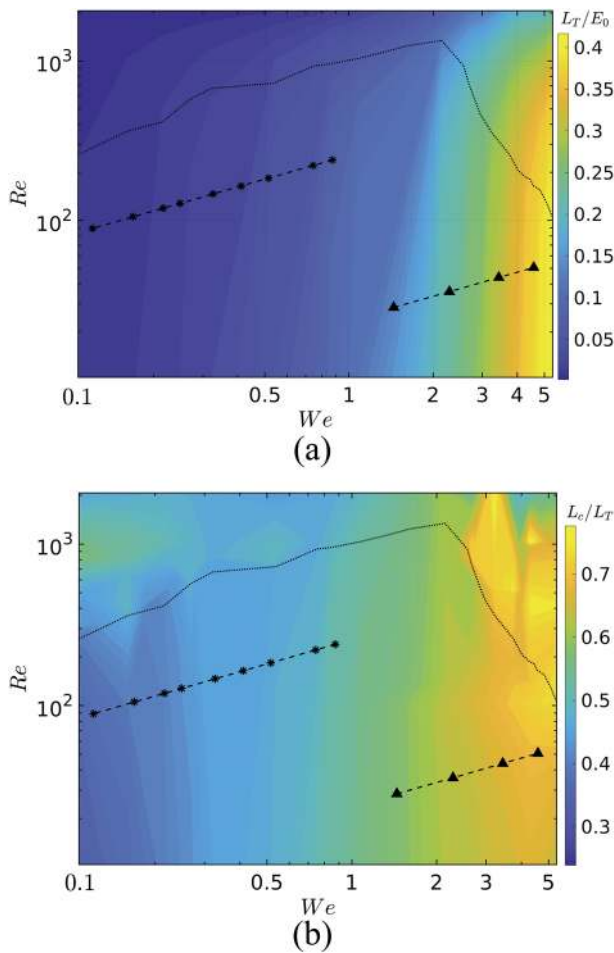


FIG. 15. Variation of (a) energy loss during one complete bouncing cycle, L_T/E_0 , and (b) relative contribution of energy loss during contact vis-à-vis total energy loss, L_c/L_T . Panel (a) shows that the maximum energy loss occurs at high Weber numbers and is only weakly dependent on the Reynolds number. Panel (b) shows that at higher Weber numbers, contact losses dominate over the energy loss that occurs during flight. The symbols correspond to experimental parameters used by de Ruiter *et al.*¹⁵ (*) and Kolinski *et al.*¹⁰ (▲).

work of Kolinski *et al.*,¹⁰ the drop assumes complex shapes, generating a great deal of internal motion inside the drop.¹³ This results in significant energy loss during contact. However, at very low We where the contact time is also very short, most of the energy is lost during flight. At $We \approx 1$, the loss of energy is nearly equipartitioned between loss during contact and loss during flight. Figure 15(b) is one of the key findings of this study and establishes the role of We unequivocally on energetics of drop impacts. The patchy region that occurs in the wettability-dependent region at high Re and We is also the region where bubble entrapment and escape occurs. Energy loss during contact in this region depends on the precise nature of the bubble entrapment process, which requires a further study.

The role of the Weber number is best illustrated by examining its effect on the drop shape during impact. We illustrate this with

one specific example taken at $Re = 51.7$ and at $We = 2.14, 3.21$. Modal decomposition is carried out by expanding the drop shape in terms of Legendre polynomials,

$$R(t, \theta) = R_0 + \sum_{n=0}^{\infty} c_n(t) P_n(\cos \theta), \quad (20)$$

where n is the mode number, $P_n(\cdot)$ is the Legendre polynomial of order n , and $c_n(t)$ is the corresponding coefficient. We use the orthogonality of the Legendre polynomials to estimate c_n in terms of drop shapes,

$$c_n(t) = \frac{2n+1}{2} \int_{-1}^1 (R(t, \theta) - R_0) P_n(\cos \theta) d(\cos \theta). \quad (21)$$

We extract the coefficients c_n for two different Weber numbers at various times, as shown in Fig. 16, for the first ten modes. At $We = 0.53$, a dominant surface mode of the drop occurs at $n = 2$, which corresponds to a prolate-oblate shape throughout the contact process, while higher modes have a significantly lower amplitude. However, at $We = 3.21$, significant energy is transferred to higher modes, which also leads to faster decay of energy

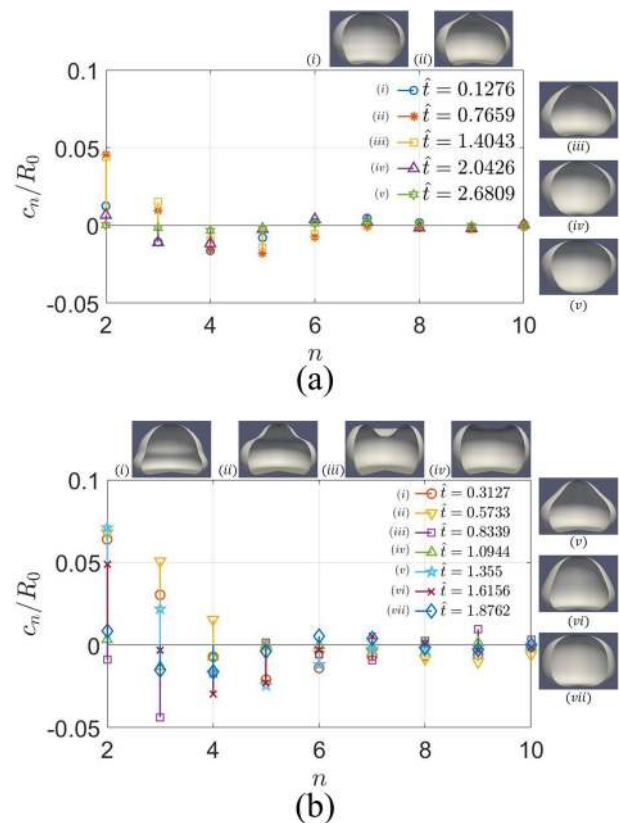


FIG. 16. Modal decomposition for two different cases: (a) $We = 0.53$, $Re = 51.7$ and (b) $We = 3.21$, $Re = 51.7$ at various times during drop evolution. For lower values of Weber numbers, the fundamental oscillation mode $n = 2$ absorbs most of the energy, whereas at higher Weber numbers, energy is distributed to higher modes too. Three-dimensional drop shapes shown in each panel correspond to the instants of time when decomposition is carried out.

of the drop at this Weber number. Prosperetti³⁰ studied the viscous decay of an oscillating drop and obtained the decay rate of surface oscillations as

$$b_0 = (n - 1)(2n + 1) \frac{\mu_l}{\rho_l R_0^2}. \quad (22)$$

This is consistent with the expression for viscous dissipation obtained by Moláček and Bush¹⁸ assuming that the flow is approximately irrotational inside the drop,

$$D = 8\pi\mu R_0^3 \sum \left(\frac{n-1}{n} \right)^2 c_n^2. \quad (23)$$

As one may expect, higher modes, indeed, decay more rapidly than lower modes as is also found in our simulations.

V. SUMMARY AND CONCLUSIONS

In the current work, we present an axisymmetric numerical study of a drop impacting a dry solid surface. In a related study by Sharma and Dixit,¹³ it was shown that drop impact dynamics can be divided into wettability-dependent and wettability-independent regimes depending on the value of Reynolds and Weber numbers. The present study explores energetics of drop impact with the aim of investigating the role of Reynolds and Weber numbers on the coefficient of restitution. A parametric study is carried out for a wide range of Re and We at fixed density and viscosity ratios. In each case, potential, kinetic, and surface energies as well as viscous dissipation are calculated for one complete bouncing cycle. A detailed energy budget is presented for two special cases at $We = 3.21$ and $Re = 207, 1035$ shown in Figs. 3 and 6. Before impact, surface energy remains constant, while gravitational potential energy is converted to kinetic energy. Due to low values of gas viscosity used in the current study (equivalent of an air–water system), viscous dissipation due to drag is negligible. The onset of impact is indicated by a steep rise in the surface energy at the expense of the drop’s kinetic energy until the drop spreads to its maximum radial extent. In the wettability-independent bouncing process where the drop is supported on a thin cushion of gas, rapid recoil occurs, resulting in a sharp decline in the surface energy. In the wettability-dependent process, recoil occurs only for hydrophobic and superhydrophobic surfaces like in the present study. Even for such impacts, the drop first spreads on a thin gas film sometimes referred to a “skating process”⁹ before contact eventually occurs. Strong shear is generated in the gas layer below, causing a large amount of viscous dissipation. The drop eventually lifts off completing the contact process. The energy loss that occurs during contact, L_c , is the major contributor in total loss, L_T , for high Weber number cases and is weakly dependent on the Reynolds number. Viscous dissipation is found to follow a simple scaling law, given by $D \sim \mu_g V_0 R_0^2 We^{1/2} St^{1/2}$. For high We and Re , bubble entrapment can often occur, as shown in Figs. 8 and 9. During this process, the drop assumes complex shapes and involves ejection of high speed jets, causing additional viscous dissipation. As the drop rises after contact, strong surface oscillations result in vigorous internal motions inside the drop. Such motions cause additional viscous dissipation, which can be obtained as $(L_T - L_c)$. As is clearly evident in Fig. 15(b), for low We , bulk of the energy loss occurs during flight, whereas at high We , bulk of the energy loss occurs during contact. This is consistent with the

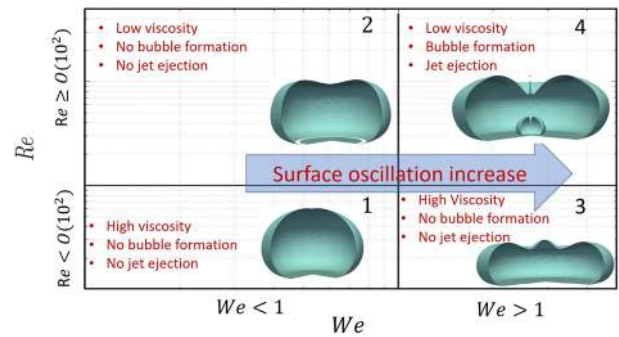


FIG. 17. A schematic view showing various types of drop–solid interactions as a function of We and Re . Physical contact with the solid surface occurs at higher values of Re , while surface-oscillation-induced dissipation occurs at higher Weber numbers. Region 4, at higher values of We and Re , corresponds to bubble entrapment cases.

experiments of Kolinski *et al.*¹⁰ carried out for $We > 1$ who noted that shear in the gas layer causes bulk of the dissipation, clearly suggesting that L_c is the dominant contributor in the total energy loss for high We impacts.

A key result of this paper is a detailed quantification of the coefficient of restitution, r_c , shown in Fig. 11. Low Weber number impacts were found to have a high value of r_c , whereas high Weber number impacts were found to have lower values of r_c . Satisfyingly, the simulations were found to be in excellent agreement with those of Kolinski *et al.*¹⁰ and de Ruiter *et al.*¹⁵ For the first time, our study systematically showed how energetics of a bouncing drop subtly depend on the value of Weber and Reynolds numbers. The main findings of this paper can be summarized with a simple schematic shown in Fig. 17.

A number of open questions remain that need careful experiments and further numerical studies. Our simulations fail to capture dynamics if gas film thicknesses reach sub-micrometer levels. For high speed impacts, it is well known that gas films can easily reach nanometer ranges where both the rarefaction and non-continuum effects become important. Their role in energetics of impact is unclear and requires further investigation. Our simulations also assume that the impact, even in wettability-dependent regimes, is axisymmetric, but a number of experiments have revealed that localized contacts first occur, and the subsequent contact line motion is highly non-axisymmetric. Roughness of the substrate is another important feature that requires further investigation, mainly with regard to its effect on the coefficient of restitution. Some of these topics are currently under investigation and will be presented in future studies.

SUPPLEMENTARY MATERIAL

See the [supplementary material](#) for a three-dimensional evolution of bubble entrapment and escape during drop impact.

AUTHORS’ CONTRIBUTIONS

H.N.D. conceptualized, defined the scope, and supervised the study. P.K.S. carried out the numerical computations. H.N.D. and

P.K.S. analyzed the data together. P.K.S. derived the scaling laws and generated all the figures and movies. H.N.D. and P.K.S. wrote this article.

ACKNOWLEDGMENTS

P.K.S. thanks the Ministry of Human Resource Development for a Ph.D. fellowship, and H.N.D. thanks the Science and Engineering Research Board (SERB), Department of Science and Technology (Grant No. ECR/2015/000086), for funding this research.

DATA AVAILABILITY

The data that support the findings of this study are available from the corresponding author upon reasonable request.

REFERENCES

- 1 A. Asai, M. Shioya, S. Hirasawa, and T. Okazaki, "Impact of an ink drop on paper," *J. Imaging Sci. Technol.* **37**, 205 (1993).
- 2 W. Bouwhuis, R. C. A. van der Veen, T. Tran, D. L. Keij, K. G. Winkels, I. R. Peters, D. van der Meer, C. Sun, J. H. Snoeijer, and D. Lohse, "Maximal air bubble entrainment at liquid-drop impact," *Phys. Rev. Lett.* **109**(26), 264501 (2012).
- 3 W. Jia and H.-H. Qiu, "Experimental investigation of droplet dynamics and heat transfer in spray cooling," *Exp. Therm. Fluid Sci.* **27**(7), 829–838 (2003).
- 4 A. L. Yarin, "Drop impact dynamics: Splashing, spreading, receding, bouncing. . ." *Annu. Rev. Fluid Mech.* **38**, 159–192 (2006).
- 5 C. Josserand and S. T. Thoroddsen, "Drop impact on a solid surface," *Annu. Rev. Fluid Mech.* **48**, 365–391 (2016).
- 6 L. Xu, W. W. Zhang, and S. R. Nagel, "Drop splashing on a dry smooth surface," *Phys. Rev. Lett.* **94**, 184505 (2005).
- 7 S. Mandre, M. Mani, and M. P. Brenner, "Precursors to splashing of liquid droplets on a solid surface," *Phys. Rev. Lett.* **102**(13), 134502 (2009).
- 8 M. Mani, S. Mandre, and M. P. Brenner, "Events before droplet splashing on a solid surface," *J. Fluid Mech.* **647**, 163–185 (2010).
- 9 J. M. Kolinski, S. M. Rubinstein, S. Mandre, M. P. Brenner, D. A. Weitz, and L. Mahadevan, "Skating on a film of air: Drops impacting on a surface," *Phys. Rev. Lett.* **108**(7), 074503 (2012).
- 10 J. M. Kolinski, L. Mahadevan, and S. M. Rubinstein, "Drops can bounce from perfectly hydrophilic surfaces," *Europhys. Lett.* **108**(2), 024001 (2014).
- 11 J. de Ruiter, R. Lagraauw, D. van den Ende, and F. Mugele, "Wettability-independent bouncing on flat surfaces mediated by thin air films," *Nat. Phys.* **11**(1), 48 (2015).
- 12 J. de Ruiter, D. van den Ende, and F. Mugele, "Air cushioning in droplet impact. II. Experimental characterization of the air film evolution," *Phys. Fluids* **27**(1), 012105 (2015).
- 13 P. K. Sharma and H. N. Dixit, "Regimes of wettability dependent and independent bouncing of a drop on a solid surface," *J. Fluid Mech.* (to be published).
- 14 D. Richard and D. Quéré, "Bouncing water drops," *Europhys. Lett.* **50**(6), 769 (2000).
- 15 J. de Ruiter, R. Lagraauw, F. Mugele, and D. van den Ende, "Bouncing on thin air: How squeeze forces in the air film during non-wetting droplet bouncing lead to momentum transfer and dissipation," *J. Fluid Mech.* **776**, 531–567 (2015).
- 16 D. Richard, C. Clanet, and D. Quéré, "Contact time of a bouncing drop," *Nature* **417**(6891), 811 (2002).
- 17 K. Okumura, F. Chevy, D. Richard, D. Quéré, and C. Clanet, "Water spring: A model for bouncing drops," *Europhys. Lett.* **62**(2), 237 (2003).
- 18 J. Moláček and J. W. M. Bush, "A quasi-static model of drop impact," *Phys. Fluids* **24**(12), 127103 (2012).
- 19 H.-Y. Kim and J.-H. Chun, "The recoiling of liquid droplets upon collision with solid surfaces," *Phys. Fluids* **13**(3), 643–659 (2001).
- 20 M. Pasandideh-Fard, S. Chandra, and J. Mostaghimi, "A three-dimensional model of droplet impact and solidification," *Int. J. Heat Mass Transfer* **45**(11), 2229–2242 (2002).
- 21 S. Chandra and C. T. Avedisian, "On the collision of a droplet with a solid surface," *Proc. R. Soc. London, Ser. A* **432**(1884), 13–41 (1991).
- 22 C. Clanet, C. Béguin, D. Richard, and D. Quéré, "Maximal deformation of an impacting drop," *J. Fluid Mech.* **517**, 199–208 (2004).
- 23 S. Popinet, "Gerris: A tree-based adaptive solver for the incompressible Euler equations in complex geometries," *J. Comput. Phys.* **190**(2), 572–600 (2003).
- 24 S. Popinet, "An accurate adaptive solver for surface-tension-driven interfacial flows," *J. Comput. Phys.* **228**(16), 5838–5866 (2009).
- 25 M. Pack, H. Hu, D. Kim, Z. Zheng, H. A. Stone, and Y. Sun, "Failure mechanisms of air entrainment in drop impact on lubricated surfaces," *Soft Matter* **13**(12), 2402–2409 (2017).
- 26 M. K. Tripathi, K. Chandra Sahu, and R. Govindarajan, "Why a falling drop does not in general behave like a rising bubble," *Sci. Rep.* **4**, 4771 (2014).
- 27 R. Manica, E. Klaseboer, and D. Y. C. Chan, "The impact and bounce of air bubbles at a flat fluid interface," *Soft Matter* **12**(13), 3271–3282 (2016).
- 28 G. B. Footte, "The water drop rebound problem: Dynamics of collision," *J. Atmos. Sci.* **32**(2), 390–402 (1975).
- 29 A. Gopinath and D. L. Koch, "Collision and rebound of small droplets in an incompressible continuum gas," *J. Fluid Mech.* **454**, 145–201 (2002).
- 30 A. Prosperetti, "Viscous effects on perturbed spherical flows," *Q. Appl. Math.* **34**(4), 339–352 (1977).